

High-harmonic generation by electric polarization, spin current, and magnetization

Tatsuhiko N. Ikeda¹ and Masahiro Sato²

¹*Institute for Solid State Physics, University of Tokyo, Kashiwa, Chiba 277-8581, Japan*

²*Department of Physics, Ibaraki University, Mito, Ibaraki, 310-8512, Japan*

(Dated: March 10, 2020)

High-harmonic generation (HHG), a typical nonlinear optical effect, has been actively studied in electron systems such as semiconductors and superconductors. As a natural extension, we theoretically study HHG from electric polarization, spin current and magnetization in magnetic insulators under terahertz (THz) or gigahertz (GHz) electromagnetic waves. We use simple one-dimensional spin chain models with or without multiferroic coupling between spins and the electric polarization, and study the dynamics of the spin chain coupled to an external ac electric or magnetic field. We map spin chains to two-band fermions and invoke an analogy of semiconductors and superconductors. With a quantum master equation and Lindblad approximation, we compute the time evolution of the electric polarization, spin current, and magnetization, showing that they exhibit clear harmonic peaks. We also show that the even-order HHG by magnetization dynamics can be controlled by static magnetic fields in a wide class of magnetic insulators. We propose experimental setups to observe these HHG, and estimate the required strength of the ac electric field E_0 for detection as $E_0 \sim 100 \text{ kV/cm} - 1 \text{ MV/cm}$, which corresponds to the magnetic field $B_0 \sim 0.1 \text{ T} - 1 \text{ T}$. The estimated strength would be relevant also for experimental realizations of other theoretically-proposed nonlinear optical effects in magnetic insulators such as Floquet engineering of magnets.

I. INTRODUCTION

Ultrafast nonlinear phenomena in condensed matter systems have recently attracted much attention owing to the development of laser science and technology¹. A remarkable example is the high-harmonic generation (HHG)² in semiconductors³. A key to this success is that strong mid-infrared laser fields have been available in recent years⁴. Since the photon energy $\hbar\Omega$ of the input laser is much smaller than the band gap, nonlinear dynamics is relevant and HHG is clearly seen⁵⁻¹⁰. Recent solid-state-HHG studies in semiconductors¹¹⁻²¹ have been extended, for example, to Dirac systems²²⁻²⁵, superconductors²⁶⁻²⁸, charge-density-wave materials^{29,30}, Mott insulators³¹⁻³³, topological insulators^{34,35}, and amorphous solids³⁶⁻³⁸.

In view of the rapid development of the HHG in electronic systems, it is natural to ask if it can be realized in spin systems (magnetic insulators) without electronic transitions. The interplay between light and magnets has been intensively studied from the viewpoints of spintronics, magnonics, magneto-optic effects, Floquet engineering, and so on. The study of visible and infrared lasers has a long history and the ultrafast spin dynamics driven by such high-frequency lasers has been long studied³⁹. On the other hand, thanks to the recent development of terahertz (THz) laser science⁴⁰⁻⁴³, magnetic dynamics driven by THz waves has been explored as well in the last decade. Since the photon energy in THz or gigahertz (GHz) range is comparable with those of magnetic excitations in magnetic insulators, such low-frequency lasers or electromagnetic waves make it possible to directly create and control magnetic excitations or states. Therefore, THz or GHz wave is necessary for mimicking HHG in semiconductors with spin systems. In fact, recently, the second harmonic generation originated from mag-

netic excitations in an antiferromagnetic insulator has been observed with an intense THz laser⁴⁴. In addition to this, various experimental studies of THz-wave driven magnetic phenomena have been done: intense THz-laser driven magnetic resonance in an antiferromagnet^{43,45}, magnon resonances in multiferroic magnets with the electric field of THz wave or laser⁴⁶⁻⁴⁸, spin control by THz-laser driven electron transitions⁴⁹, dichroisms driven by THz vortex beams in a ferrimagnet⁵⁰, etc. These experimental studies have stimulated theorists in many fields of condensed-matter physics, and as a result, several ultrafast magnetic phenomena driven by THz or GHz waves have been proposed and predicted: THz-wave driven inverse Faraday effect^{51,52}, Floquet engineering of magnetic states such as chirality ordered states⁵³ and a spin liquid state⁵⁴, applications of topological light waves to magnetism⁵⁵⁻⁵⁸, control of exchange couplings in Mott insulators with low-frequency pulses^{59,60}, optical control of spin chirality in multiferroic materials⁶¹, and rectification of dc spin currents in magnetic insulators with THz or GHz waves^{62,63}. Very recently, Takayoshi et al.⁶⁴ numerically calculate the HHG spectra in quantum spin models, assuming that the applied THz laser is extremely strong beyond the current technique.

Despite of these activities, it is still difficult to realize a sufficiently strong laser-spin coupling in the THz and GHz regimes. A main reason for the difficulty is that the field amplitude of THz laser pulse is quite limited (at most the order of 1 MV/cm) compared with the visible and the mid-infrared lasers. In addition, electromagnetism tells us that the light-spin coupling is generally smaller than the light-charge one roughly by a factor of c^{-1} with c being the speed of light. Therefore, to find practical experimental ways of HHG in spin systems, it is important to study how easy or difficult it is to observe the HHG with a moderate field strength at

the frequency as large as the spin gap. The long study of magnetic resonances shows that, when THz or GHz wave at adjusted frequency Ω is applied to magnetic insulators, we can usually obtain a clear linear response signal. Thus the question is whether significant signals at $n\Omega$ ($n = 2, 3, \dots$) appear as the nonlinear response to THz fields with moderate strength.

From the experimental viewpoint, the HHG may be one of the simplest phenomena in nonlinear optical effects in magnetic insulators. Therefore, estimating required strength of THz or GHz waves for the HHG contributes not only to deepen the understanding of the HHG itself, but also to give us a reference value of required ac fields for the realization of the other nonlinear phenomena such as optical control of magnetism^{55,56,61}, Floquet engineering of magnets^{51–54}, and spin current rectification^{62,63}.

In this paper, we theoretically study harmonic generation and harmonic spin currents in magnetic insulators with ac electric and magnetic fields within the reach of current technology. We take account of relaxation of magnetic excitations and investigate their dynamics by means of a quantum master equation, showing that clear harmonic signals are present at reasonable field strengths. We show that the photon energy $\hbar\Omega$ of the driving field does not need to be much smaller than the spin gap if the relaxation is relevant as is typically the case with magnetic insulators. This finding implies that a wider class of THz and GHz electromagnetic waves are useful to experimentally observe nonlinear optical effects in magnetic insulators.

The rest of this paper is organized as follows. In Sec. II, we introduce an inversion-asymmetric spin chain as a simple realistic model for multiferroic or standard magnetic insulators in order to study harmonic responses of electric polarization and spin current. We transform this model into that of fermions with two energy bands like semiconductors, and formulate our quantum master equation, which describes dynamics in the presence of relaxation. On the basis of this formulation, we investigate the dynamics and its Fourier spectra of electric polarization and spin current in Secs. III and IV, respectively. Thanks to the introduction of relaxation into the master equation, those spectra are well-defined without artificial treatment such as window functions. We show that harmonic generation and harmonic spin currents can be produced and detectable by using currently available lasers. In Sec. V, we introduce an anisotropic model including the transverse-field Ising model in order to study harmonic generation through nonlinear magnetization dynamics. This model can be mapped to a fermionic BCS-type Hamiltonian of superconductors, and our quantum master equation is also applicable. We thereby conduct a parallel analysis, showing that harmonic generation is possible through magnetization. We also show that the SHG can be controlled by static magnetic fields. In Sec. VI, we discuss how to experimentally detect the harmonic generation and the harmonic spin currents. In the above sections, we mainly focus on rel-

atively low-order harmonics ($n = 2, 3, 4, 5$), which could be observable with the currently available laser strength even though the laser-spin coupling is weak in principle. In Sec. VII, we study the harmonic spectra under hypothetical strong fields of theoretical interest. We thereby discuss the correspondence between the spin system and semiconductors or superconductors at the level of the harmonic spectra. Finally, in Sec. VIII, we summarize our results and make concluding remarks.

II. SETUP FOR ELECTRIC POLARIZATION AND SPIN CURRENT

A. Model and Observables

To study nonlinear dynamics of electric polarization and spin current, we consider a simple spin model in one dimension. The Hamiltonian is given by

$$\hat{H}_I = \hat{H}_{XX} + \hat{H}_{\text{stag}}, \quad (1)$$

with

$$\begin{aligned} \hat{H}_{XX} &= J \sum_{j=1}^{2L} (\hat{S}_j^x \hat{S}_{j+1}^x + \hat{S}_j^y \hat{S}_{j+1}^y), \\ \hat{H}_{\text{stag}} &= \sum_{j=1}^{2L} (-1)^j \left[J_{\text{stag}} (\hat{S}_j^x \hat{S}_{j+1}^x + \hat{S}_j^y \hat{S}_{j+1}^y) + H_{\text{stag}} \hat{S}_j^z \right], \end{aligned} \quad (2)$$

where $\hat{S}_j^\alpha = \sigma_j^\alpha / 2$ ($\alpha = x, y$, and z) are the spin operators at site j with σ_j^α being the Pauli matrices. Here \hat{H}_{XX} represents the isotropic XY model with exchange coupling J , and \hat{H}_{stag} consists of the staggered exchange coupling J_{stag} and the staggered Zeeman coupling H_{stag} . The number of sites is $2L$, and the periodic boundary condition is imposed.

The Hamiltonian (1) is a simple but realistic model for one-dimensional quantum magnets. In fact, the staggered exchange coupling J_{stag} often appears in spin Peierls magnets such as CuGeO_3 ^{65–70} and TTF-CA ^{71–73}. The staggered field term H_{stag} ^{74–76} is known to exist in a class of two-sublattice spin chain compounds such as Cu-benzoate ⁷⁷, $[\text{PMCu}(\text{NO}_3)_2(\text{H}_2\text{O})_2]_n$ (PM=pyrimidine)⁷⁸, KCuGaF_6 ^{79,80}, KCuMoO_4OH ⁸¹, and Yb_4As_3 ⁸².

The symmetries of the Hamiltonian (1) are as follows. Both the bond-center and site-center inversion symmetries are broken if both J_{stag} and H_{stag} are nonzero. These inversion-symmetry-breaking terms are very important to consider the HHG spectra because even-order HHG signals ($n\Omega$ with $n = 2, 4, 6, \dots$) generally disappear in inversion-symmetric systems⁸³. Note that the Hamiltonian (1) has the global $U(1)$ symmetry around the S^z -axis and the total magnetization $\sum_j \hat{S}_j^z$ is conserved. In Sec. V, we switch to another Hamiltonian, for

which it is not conserved, and discuss the magnetization dynamics and harmonic generation.

We describe the laser-spin coupling by either of the following two effects. The first one is the Zeeman coupling to the laser magnetic field $B(t)$ along the S^z direction, $\hat{H}_{\text{ext}}^Z(t) = -B(t) \sum_j [\eta_Z^u + (-1)^j \eta_Z^s] \hat{S}_j^z$. Here $\eta_Z^u = g\mu_B$, g is the g factor, μ_B the Bohr magneton, and we set $\hbar = 1$ throughout this paper. We assume that $\eta_Z^s \neq 0$ when we consider \hat{H}_I because the magnetic field acting on site j is modified in general by the inner magnetic field. The part of $-\eta_Z^s B(t) \sum_j \hat{S}_j^z$ causes no physical effect because the total magnetization is also conserved in the presence of $B(t)$. Thus, when we consider \hat{H}_I , we will use

$$\hat{H}_{\text{ext}}^Z(t) = -b(t) \sum_j (-1)^j \hat{S}_j^z \quad (4)$$

with $b(t) \equiv B(t)\eta_Z^s$.

The second laser-spin coupling is the so-called magnetostriction effect⁸⁴. This is the coupling of the laser electric field $E(t)$ to the spin-dependent electric polarization proportional to $\hat{\mathbf{S}}_j \cdot \hat{\mathbf{S}}_{j+1}$. We write the coupling term as $-E(t) \sum_j [\eta_{\text{MS}}^u + (-1)^j \eta_{\text{MS}}^s] (\hat{S}_j^x \hat{S}_{j+1}^x + \hat{S}_j^y \hat{S}_{j+1}^y)$. We have assumed that the dot product $\hat{\mathbf{S}}_j \cdot \hat{\mathbf{S}}_{j+1}$ is dominated by $\hat{S}_j^x \hat{S}_{j+1}^x + \hat{S}_j^y \hat{S}_{j+1}^y$ correspondingly to our Hamiltonian (1). Here η_{MS}^u is a constant converting the spin dot product into the polarization, and η_{MS}^s is its staggered counterpart. We note that η_{MS}^s is larger than η_{MS}^u in typical multiferroic materials^{46-48,84}, and thus neglect η_{MS}^u for simplicity. The coupling Hamiltonian is therefore given, in this work, by

$$\hat{H}_{\text{ext}}^{\text{MS}}(t) = -e(t) \sum_j (-1)^j (\hat{S}_j^x \hat{S}_{j+1}^x + \hat{S}_j^y \hat{S}_{j+1}^y) \quad (5)$$

with $e(t) \equiv E(t)\eta_{\text{MS}}^s$.

The electric polarization

$$\hat{P} = \eta_{\text{MS}}^s \sum_j (-1)^j (\hat{S}_j^x \hat{S}_{j+1}^x + \hat{S}_j^y \hat{S}_{j+1}^y) \quad (6)$$

is the first observable of interest. When its expectation value evolves in time as $P(t) = \langle \hat{P} \rangle_t$, it becomes the source of electromagnetic radiation, which is useful for the experimental detection. The radiation power at frequency ω is given by

$$I_P(\omega) \propto |\omega^2 P(\omega)|^2, \quad (7)$$

where $P(\omega)$ is the Fourier transform of $P(t)$. Before the application of laser, the expectation value of the polarization $P_0 = \langle \hat{P} \rangle_{t_{\text{ini}}}$ is generally nonzero. Since a constant shift of $P(t)$ does not change $I_P(\omega)$, we will also use $\Delta P(t) = P(t) - P_0$. In the following, we show that $I_P(\omega)$ exhibits several peaks at integer multiples of the driving frequency, which correspond to the HHG.

We remark that the even-order HHG vanishes for $J_{\text{stag}} = 0$, at which the system Hamiltonian \hat{H}_I is invariant whereas the polarization \hat{P} is odd under the (site-center) inversion. This is exactly the same selection rule

for the ‘‘conventional’’ HHG in inversion-symmetric semiconductors. The selection rule is understood in the perturbation regime as follows. For instance, the second harmonic derives from $P(2\Omega) = \chi^{(2)} E_\Omega E_\Omega$, where $\chi^{(2)}$ is the nonlinear susceptibility and E_Ω is the Fourier component of the input field (see a textbook⁸⁵ for more rigorous discussions). By applying the inversion, we also have $-P(2\Omega) = \chi^{(2)} E_\Omega E_\Omega$, where we have used the invariance of $\chi^{(2)}$ in inversion-symmetric systems. The above two equations imply that $\chi^{(2)}$ and hence $P(2\Omega)$ vanish in inversion-symmetric systems. Similar arguments hold true for all the even-order HHGs, which thus vanish in inversion-symmetric systems. Note that such constraints are not obtained for the odd-order HHGs that in fact exist both inversion-symmetric and -asymmetric systems.

The spin current is the second observable of interest. This is defined through the continuity equation for \hat{S}_j^z , and its definition depends on the coupling term. When we consider the total Hamiltonian $\hat{H}_I + \hat{H}_{\text{ext}}^Z(t)$, the spin current operator is given by

$$\hat{J}_{\text{spin}} = \sum_j [J + (-1)^j J_{\text{stag}}] (\hat{S}_j^x \hat{S}_{j+1}^y - \hat{S}_j^y \hat{S}_{j+1}^x). \quad (8)$$

On the other hand, when we consider the total Hamiltonian $\hat{H}_I + \hat{H}_{\text{ext}}^{\text{MS}}(t)$, it is given by

$$\hat{J}_{\text{spin}} = \sum_j \{J + (-1)^j [J_{\text{stag}} - e(t)]\} (\hat{S}_j^x \hat{S}_{j+1}^y - \hat{S}_j^y \hat{S}_{j+1}^x). \quad (9)$$

Both Eqs. (8) and (9) are odd under the inversion like the electric current in semiconductors, and the even-order harmonics vanish when the system is inversion-symmetric (the above argument on the polarization applies equally). We will see, in Sec. II B, the spin currents in our setup are analogous to the charge currents in semiconductors.

Whereas the electric polarization is measured as the radiation from it, the spin current is usually measured through conversion to an electric current. Thus, in discussing the spin current, we use the Fourier component $J_{\text{spin}}(\omega)$ by itself, rather than the radiation power such as Eq. (7).

B. Fermionization

Our spin model can be mapped to noninteracting spinless fermions by means of the Jordan-Wigner transformation⁸⁶: $\hat{S}_j^+ = \prod_{i(<j)} (1 - 2\hat{c}_i^\dagger \hat{c}_i) \hat{c}_j$, $\hat{S}_j^- = \prod_{i(<j)} (1 - 2\hat{c}_i^\dagger \hat{c}_i) \hat{c}_j^\dagger$, and $\hat{S}_j^z = 1/2 - \hat{c}_j^\dagger \hat{c}_j$ with $\hat{S}_j^\pm = (\hat{S}_j^x \pm i\hat{S}_j^y)/2$. The Hamiltonian (1) is simplified by introducing the following Fourier transformations for the odd and even sites:

$$\hat{a}_k \equiv \frac{1}{\sqrt{L}} \sum_{j=1}^L e^{-ik(2j)} \hat{c}_{2j}; \quad \hat{b}_k \equiv \frac{1}{\sqrt{L}} \sum_{j=1}^L e^{-ik(2j+1)} \hat{c}_{2j+1} \quad (10)$$

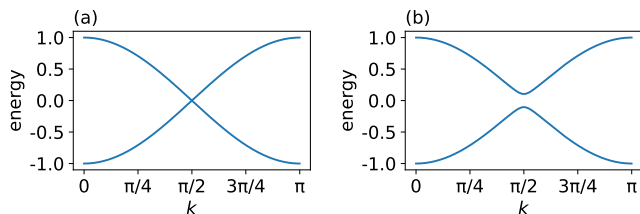


FIG. 1. Band structure of Jordan-Wigner fermions for (a) the inversion-symmetric model \hat{H}_{XX} and (b) the inversion-asymmetric model $\hat{H}_{XX} + \hat{H}_{\text{stag}}$ with asymmetric parameters $(J_{\text{stag}}, H_{\text{stag}}) = (0.1, 0.03)$. The unit of energy is taken as $J = 1$.

with $k = \pi m/L$ ($m = 0, 1, \dots, L-1$). By introducing the two-component fermion operator $\phi_{1,k} \equiv {}^t(\hat{a}_k, \hat{b}_k)$, one obtains

$$\hat{H}_I = \sum_k \phi_{1,k}^\dagger H_I(k) \phi_{1,k}, \quad (11)$$

where $H_I(k)$ is a 2×2 matrix representation in our basis and given by

$$H_I(k) = J \cos k\sigma_x - J_{\text{stag}} \sin k\sigma_y - H_{\text{stag}}\sigma_z. \quad (12)$$

The two eigenvalues of $H_I(k)$ are $\pm\epsilon_1(k)$ with $\epsilon_1(k) = \sqrt{(J \cos k)^2 + (J_{\text{stag}} \sin k)^2 + H_{\text{stag}}^2}$, which define the two energy bands. Thus the band gap, i.e. spin gap, is given by

$$\Delta_I = 2\sqrt{J_{\text{stag}}^2 + H_{\text{stag}}^2}, \quad (13)$$

where J_{stag} and H_{stag} are assumed to be smaller enough than J . The band structures are illustrated in Fig. 1.

We then fermionize the laser-matter couplings and the observables, and make the 2×2 -matrix representations in our basis. The coupling terms are given by

$$H_{\text{ext}}^Z(k, t) = b(t)\sigma_z, \quad (14)$$

$$H_{\text{ext}}^{\text{MS}}(k, t) = e(t) \sin k\sigma_y, \quad (15)$$

and the electric polarization reads

$$P(k) = -\eta_{\text{MS}}^s \sin k\sigma_y. \quad (16)$$

The spin current depends on the coupling term, and its matrix representation is given, for the Zeeman coupling, by

$$J_{\text{spin}}(k) = J \sin k\sigma_x + J_{\text{stag}} \cos k\sigma_y, \quad (17)$$

and, for the magnetostriction effect, by

$$J_{\text{spin}}(k, t) = J \sin k\sigma_x + [J_{\text{stag}} - e(t)] \cos k\sigma_y. \quad (18)$$

We remark that, in the fermion representation, our model is analogous to two-band models used in the HHG

studies for itinerant electrons. For itinerant electrons, the laser electric field causes the intraband acceleration and the interband transition, both of which play important roles in the HHG. In our model, both \hat{H}_{ext}^Z and $\hat{H}_{\text{ext}}^{\text{MS}}$ involve the interband and the intraband effects. To see this, we first consider the special case of $J_{\text{stag}} = H_{\text{stag}} = 0$, where $H_I(k) = J \cos k\sigma_x$. Making a unitary transformation U_0 , we diagonalize this Hamiltonian as $H_I(k)' = J \cos k\sigma_z$, where the coupling terms are represented as $H_{\text{ext}}^Z(k, t)' = b(t)\sigma_y$ and $H_{\text{ext}}^{\text{MS}}(k, t)' = e(t) \sin k\sigma_x$. It is manifest that the coupling terms have nonzero elements only in the off-diagonal components, and thus lead to interband transitions and have no intraband effect. Next we consider the case of $J_{\text{stag}} \neq 0$ or $H_{\text{stag}} \neq 0$, where the unitary transformation U_1 diagonalizing $H_I(k)$ is different from U_0 . Thus, in the energy eigenbasis, the coupling terms have, in general, diagonal elements, and some intraband effects are involved. Although the details such as the k -dependence are different, we expect that the intra- and interband effects in our model result in the HHG. In fact, as we will see at the ends of Secs. III and IV, the harmonic spectra are analogous to those of semiconductors.

C. Time Evolution and Laser Pulse

We suppose that the system is initially in the ground state $|\psi_{\text{gs}}\rangle = \otimes_k |\phi_g(k)\rangle$ and the laser magnetic or electric field is turned off. In terms of the fermion representation, the ground state is the one where the lower energy band is fully occupied and the upper one is completely unoccupied.

The time evolution is caused by either magnetic field $b(t)$ or electric field $e(t)$. Sufficiently strong field amplitudes ($\sim 1\text{MV/cm}$) at THz regime are obtained for pulse lasers^{40,42,43} and it is still difficult to generate THz continuous waves with high intensity. Therefore, we consider $b(t)$ and $e(t)$ of pulse shape:

$$b(t) = b_0 \cos(\Omega t) f(t); \quad e(t) = e_0 \cos(\Omega t) f(t). \quad (19)$$

Here b_0 and e_0 are the peak coupling energy, Ω is the central frequency, and $f(t)$ is the Gaussian envelope function, $f(t) = \exp[-2 \ln 2 (t^2/t_{\text{FWHM}}^2)]$, where t_{FWHM} represents the full width at half maximum of the intensity $e(t)^2$ or $b(t)^2$. We refer to t_{FWHM}/T with $T \equiv 2\pi/\Omega$ as the number of cycles of the pulse field, which is assumed to be 5 unless otherwise specified below.

As emphasized in Sec. I, relaxation is important in our setup because its timescale is comparable to the periods of THz and GHz waves. To take account of this effect, we describe the time evolution by a quantum master equa-

tion of the Lindblad form⁸⁷:

$$\begin{aligned} \frac{d}{dt}\rho(k, t) = & -i[H(k, t), \rho(k, t)] \\ & + \gamma \left(L_k \rho(k, t) L_k^\dagger - \frac{1}{2} \{L_k^\dagger L_k, \rho(k, t)\} \right), \end{aligned} \quad (20)$$

where $\rho(k, t)$ is the 2×2 reduced density matrix for the subspace with wave number k . Here the Lindblad operator $L_k \equiv |\phi_g(k)\rangle \langle \phi_e(k)|$ describes the relaxation from the excited state $|\phi_e(k)\rangle$ to the ground state $|\phi_g(k)\rangle$, and γ does its rate. For simplicity, we assume that γ is independent of k and set $\gamma = 0.1J$. This relaxation rate corresponds to the lifetime $\tau = \gamma^{-1} \sim 7.6$ ps (1.5 ps) for a typical exchange interaction $J/k_B = 10$ K (50 K).

Our master equation (20) ensures that the system relaxes to the ground state in the long run after the external field is switched off. Without relaxation, the system would remain excited in an infinitely long time after the pulse irradiation. We will see later that our master equation approach thereby allows us to obtain well-defined Fourier spectra of observables without artificial treatment such as window functions.

In solving the quantum master equation (20), we take the initial condition $\rho(k, t_{\text{ini}}) = |\phi_g(k)\rangle \langle \phi_g(k)|$ with the initial time $t_{\text{ini}} (< 0)$ being so small that $f(t_{\text{ini}}) \simeq 0$. At time t , the expectation value of an observable

$$\hat{O} = \sum_k \phi_{I,k}^\dagger \mathcal{O}(k) \phi_{I,k}, \quad (21)$$

is given by

$$O(t) = \langle \hat{O} \rangle_t = \sum_k \text{tr}[\rho(k, t) \mathcal{O}(k)]. \quad (22)$$

D. Units and Scales of Physical Quantities

Before discussing our results, we make remarks on the scales of physical quantities. In the following, we work in the units with $J = 1$ and represent all physical quantities including the photon energy, the lifetime of the magnetic excitation, and the magnetic and the electric fields, in a dimensionless manner with the physical constants set to unity. The rules to recover the units depend on the value of J that we suppose. In Table I, we provide the rules for the two choices of $J = 10$ K and 50 K, which are typical energy scales of magnets. In this table, we have assumed that $\eta_Z^s = g\mu_B$ and $\eta_{\text{MS}}^s = g\mu_B/c$, where c is the speed of light. The second assumption implies that, in good multiferroic materials, the magneto-electric coupling is as large as the Zeeman coupling^{84,88–90}.

We also provides two tables for convenience. Table II is the unit conversion table between different physical quantities. Table III shows the correspondence between the electric-(magnetic-)field amplitude and the energy flux.

As we noted in Introduction, the maximum intensity of the THz waves (~ 1 MV/cm) is typically smaller than

that of the mid- and near-infrared lasers used in HHG measurements in semiconductors. Table I tells us that this corresponds to $\sim 0.1J$ at most. Therefore we will mainly focus on relatively lower-order ($n = 2, 3, 4, 5$) harmonics in Secs. III–VI.

III. ELECTRIC POLARIZATION

In this section, we discuss the high-harmonic spectrum of the electric polarization. We use the Hamiltonian \hat{H}_I (1), and discuss the effects of driving by either \hat{H}_{ext}^Z (4) or $\hat{H}_{\text{ext}}^{\text{MS}}$ (5). As discussed in Sec. IID, we work in the dimensionless units corresponding to Table I.

TABLE I. Table of units for physical parameters depending on two choices of $J = 10$ K and 50 K.

Energy, J	10 K	50 K
Photon energy, $\hbar\Omega$	0.86 meV	4.3 meV
Time, \hbar/J	0.76 ps	0.15 ps
Frequency, $f = \Omega/(2\pi)$	0.21 THz	1.0 THz
Magnetic field, $B_0 = J/(g\mu_B)$	7.4 T	37 T
Electric field, $E_0 = cB_0$	22 MV/cm	112 MV/cm

TABLE II. Unit conversion table.

EM field	THz	GHz
Frequency, $\Omega/(2\pi)$	10^{12} Hz	10^9 Hz
Energy, $\hbar\Omega$	4.1 meV	4.1 μ eV
Temperature, $T = \hbar\Omega/k_B$	48 K	48 mK
Magnetic field, $B_0 = \hbar\Omega/g\mu_B$	36 T	36 mT
Electric field, $E_0 = cB_0$	107 MV/cm	107 kV/cm

TABLE III. Laser energy flux for reference field strengths.

$E_0 = 1$ MV/cm	
Magnetic field, B_0	0.33 T
Energy flux, I	1.3 GW/cm ²

We first investigate the typical behaviors of the time profile $\Delta P(t)$ and the corresponding power spectrum $I_P(\omega)$ (7) obtained by \hat{H}_{ext}^Z (4). Figure 2 shows the results obtained for the parameters $J_{\text{stag}} = 0.1$, $H_{\text{stag}} = 0.03$, and $B_0\eta_Z^s = 0.02$, with several driving frequencies. Here the power spectrum is normalized so that the fundamental harmonic $I_P(\Omega)$ is unity. We note that the even-order harmonics are present since the inversion symmetry is broken now.

The lowest frequency $\Omega = 0.02$, which is approximately 10 times smaller than the spin gap $\Delta_I = 0.21$, corresponds to the standard setup for the semiconductor HHG and the previous study of spin-system HHG⁶⁴. At this lowest frequency, strong harmonic peaks are obtained and the peak heights slowly decrease as the harmonic order increases. At this frequency, $\Omega \ll \gamma^{-1}$ holds, and thus the dynamics is nearly adiabatic. Namely, relaxation occurs so fast that the quantum state always ap-

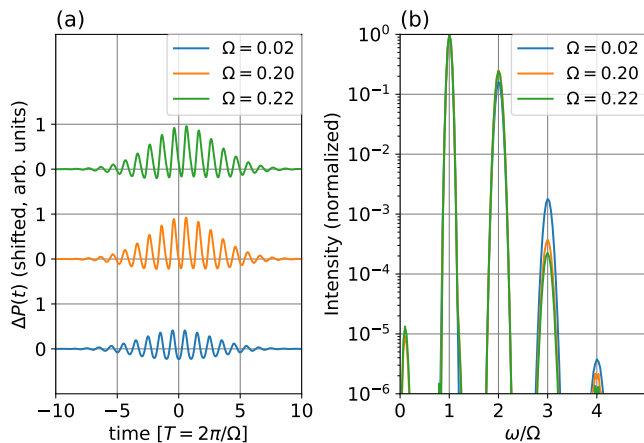


FIG. 2. (a) Time profile of $\Delta P(t)$ for the Zeeman driving $\hat{H}_{\text{ext}}^Z(t)$ with frequency $\Omega = 0.02, 0.2$, and 0.22 . The parameters are $J_{\text{stag}} = 0.1$, $H_{\text{stag}} = 0.03$, and $b_0 = 0.02$, where the spin gap is $\Delta_I = 0.21$. (b) Corresponding power spectrum $I_P(\omega)$ (7) plotted against ω/Ω .

proaches to ground state at the instantaneous external field.

The harmonic peaks are present regardless of whether the driving frequency is well below the gap or near-resonant. In fact, in Fig. 2(b), we find strong harmonic peaks for $\Omega = 0.20$ and 0.22 , which are slightly below and above the spin gap $\Delta_I = 0.21$, respectively. At these frequencies $\Omega \sim \gamma^{-1}$, the quantum dynamics is more coherent than that for $\Omega = 0.02$ (i.e., less suffers from the environment), but the relaxation is still effective to keep harmonic peaks strong and sharp. Regarding experiments with THz laser pulse, it is advantageous that the harmonics peaks are seen with higher frequencies because the spin gap is typically smaller than 1THz-photon energy in many of magnetic insulators and it becomes more difficult to obtain high field amplitudes in the frequency regime lower than 1THz.

Now we systematically investigate the intensity of the second- and third-harmonic generation (SHG and THG). We fix $H_{\text{stag}} = 0.03$ and $\Omega = 0.5$, and calculate the harmonic spectrum for various sets of parameters (b_0, J_{stag}) . Figures 3(a) and (b) respectively show $I_P(2\Omega)$ and $I_P(3\Omega)$ driven by the ac Zeeman coupling $\hat{H}_{\text{ext}}^Z(t)$. Here the unit of the intensity is chosen as the fundamental harmonic $I_P(\Omega)$ for $b_0 = J_{\text{stag}} = 0.05$. Both the SHG and the THG tend to increase as b_0 or J_{stag} increases, and these signals can be as large as the fundamental harmonic. It is very natural that the HHG signal grows up with the increase of the light-spin coupling b_0 . Moreover, the growth of SHG with the increase of J_{stag} is easily understood because the inversion symmetry is broken by the presence of both J_{stag} and H_{stag} , and the SHG disappears in inversion-symmetric systems. In fact, we have confirmed that in the limit of $J_{\text{stag}} \rightarrow 0$, where the site-center inversion symmetry recovers, the SHG vanishes in

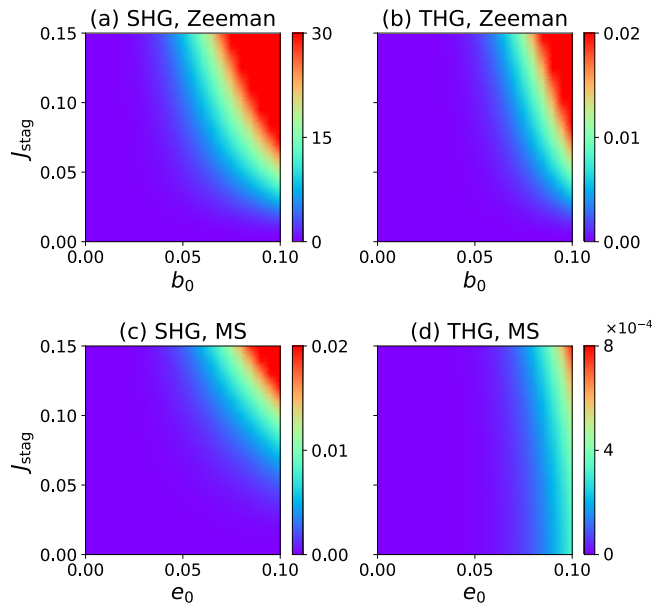


FIG. 3. Intensities of SHG [$I_P(2\Omega)$] (left) and THG [$I_P(3\Omega)$] (right) from electric polarization driven by ac Zeeman coupling (upper) and magnetostriction effect (lower) at $\Omega = 0.5$. The unit of intensity in panels (a) and (b) is chosen as $I_P(\Omega)$ for $b_0 = J_{\text{stag}} = 0.05$, and that in panels (c) and (d) as $I_P(\Omega)$ for $e_0 = J_{\text{stag}} = 0.05$. The other parameters are set as $\gamma = 0.1$ and $H_{\text{stag}} = 0.03$. The ratio of the two units, $I_P(\Omega)_{b_0=J_{\text{stag}}=0.05}/I_P(\Omega)_{e_0=J_{\text{stag}}=0.05}$, is 1.4×10^{-3} . Namely, the fundamental harmonic for the magnetostriction is much larger than that for the Zeeman coupling.

line with the selection rule.

HHG is also obtained by the magnetostriction effect $\hat{H}_{\text{ext}}^{\text{MS}}(t)$. Figures 3(c) and (d) respectively show $I_P(2\Omega)$ and $I_P(3\Omega)$ in the (e_0, J_{stag}) plane, where we again fix $H_{\text{stag}} = 0.03$ and $\Omega = 0.5$. As we already mentioned, the coupling constant e_0 can be as large as the ac Zeeman one b_0 in multiferroic magnets, and we thereby set the maximum value of e_0 to be that of b_0 in Fig. 3. Compared with (a) and (b), the panels (c) and (d) seem to imply that the SHG and the THG by the magnetostriction effect are much smaller than those by the ac Zeeman coupling. However, this is mainly because the fundamental harmonic $I_P(\Omega)$ is quite large for the magnetostriction case, and the absolute values of the SHG and the THG are comparable in the two cases.

In addition to $\Omega = 0.5$, we have investigated $\Omega = 0.2$, which is closer to the spin gap (data not shown). In this case, the signals tend to become large when the spin gap approaches the photon energy $\hbar\Omega$. In this parameter region, we have confirmed that the absolute values of the SHG and the THG are somewhat larger for the magnetostriction effect than for the ac Zeeman coupling.

Let us estimate the required laser-field amplitudes to observe HHG in experiments (see Sec. VI for experimental protocols). Considering a recent experiment in an an-

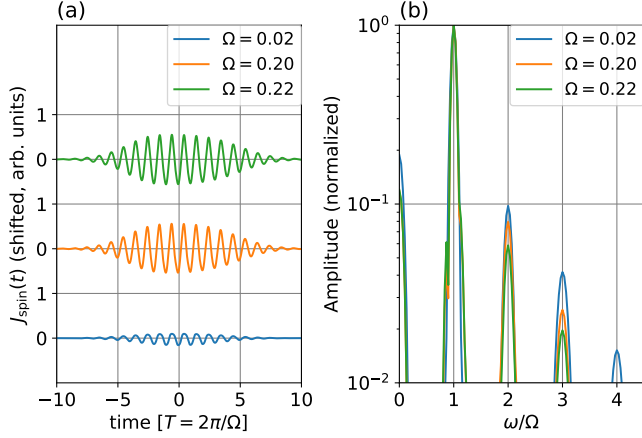


FIG. 4. (a) Time profile of $J_{\text{spin}}(t)$ for the ac Zeeman driving $\hat{H}_{\text{ext}}^Z(t)$ with frequency $\Omega = 0.02, 0.2$, and 0.22 . The parameters are $J_{\text{stag}} = 0.1$, $H_{\text{stag}} = 0.03$, and $b_0 = 0.1$, where the spin gap is $\Delta_I = 0.21$. (b) Corresponding amplitude spectrum $|J_{\text{spin}}(\omega)|$ (7) plotted against ω/Ω .

tiferromagnetic crystal⁴⁴, we suppose that a 1% intensity (10% amplitude) of the fundamental harmonic is actually detectable. We apply this criterion to our calculations for $J_{\text{stag}} = 0.05$ and $H_{\text{stag}} = 0.03$ at $\Omega = 0.5$, which corresponds to $f = 0.10$ THz (0.52 THz) for magnets of energy scale $J = 10$ K (50 K) (see Table I). As for the ac Zeeman driving with, e.g., $b_0 = 0.01$, the SHG has about a 10% intensity of the fundamental harmonic and should be observable whereas the THG does about a 10^{-4} intensity and its detection might be challenging. Thus we regard $b_0 = 0.01$ as a required field amplitude to observe HHG in experiments. According to Table I, this field amplitude corresponds to $B_0 = 74$ mT (370 mT) for magnets of energy scale $J = 10$ K (50 K). From Table III, this magnetic field amplitude corresponds to the electric field amplitude $E_0 = 220$ kV/cm (1.1 MV/cm) and the energy flux $I = 0.29$ GW/cm² (1.5 GW/cm²). These field amplitudes are within the reach of the current THz-laser technology^{40–43}. As for the magnetostriction effect, the required amplitude is larger than the above values by some factor.

IV. SPIN CURRENT

In this section, we investigate the harmonic spectrum of the spin current. As in the previous section, we use the Hamiltonian \hat{H}_I (1) and consider the effects of driving by either \hat{H}_{ext}^Z (4) or $\hat{H}_{\text{ext}}^{\text{MS}}$ (5).

The ac Zeeman driving \hat{H}_{ext}^Z (4) gives rise to harmonic peaks in the spin-current spectrum $|J_{\text{spin}}(\omega)|$ similarly to the electric polarization. Figure 4 shows the typical time profile $J_{\text{spin}}(t)$ and spectrum $|J_{\text{spin}}(\omega)|$, where the parameters are the same as in Fig. 2. Here the spectrum is

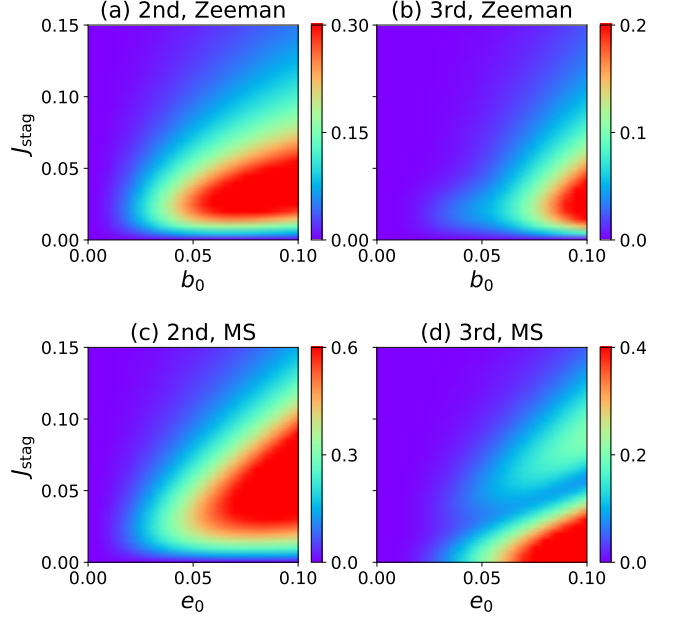


FIG. 5. Intensities of second- [$|J_{\text{spin}}(2\Omega)|$] (left) and third-harmonic spin currents [$|J_{\text{spin}}(3\Omega)|$] (right) by the ac Zeeman coupling (upper) and the magnetostriction effect (lower). The unit of intensity is chosen as $|J_{\text{spin}}(\Omega)|$ for b_0 (e_0) = $J_{\text{stag}} = 0.05$. The other parameters are set as $\gamma = 0.1$, $H_{\text{stag}} = 0.03$, and $\Omega = 0.02$.

normalized so that the fundamental harmonic $|J_{\text{spin}}(\Omega)|$ is unity. Again, the clear peaks are observable both for $\omega = 0.02 \sim 0.1\Delta_I$ and $\omega \sim \Delta_I$.

We note that there also exists the dc ($\omega = 0$) component of the spin current. As was proposed in Refs.^{62,63}, this corresponds to the rectification of the spin current, which occurs in inversion-asymmetric magnets. For $\Omega = 0.2$ and 0.22 , the peak heights of $\omega = 0$ and $\omega = 2\Omega$ are similar as shown in Fig. 4(b). Thus, if the spin-current rectification is observed in an experiment, the second harmonic is also likely to be observed in the experimental setup.

The peak heights of the second and the third harmonics are systematically shown in Fig. 5 for the ac Zeeman coupling and the magnetostriction effect as was done for the electric polarization in the previous section. Here we use a lower frequency $\Omega = 0.02$, which corresponds to $f = 4.2$ GHz (21 GHz) for magnets of energy scale $J = 10$ K (50 K) (see Table I). This lower frequency is advantageous in experimentally observing the spin currents in electric circuits because the upper limit of the frequency Ω for the electric detection is in a GHz regime⁹¹. In Sec. VI, we will discuss in detail how high harmonic spin currents are observed by electric techniques.

The second harmonic spin current exhibits a nonmonotonic behavior as a function of J_{stag} while monotonically increases with b_0 or e_0 as shown in the panels (a) and (c). This nonmonotonic behavior arises from the follow-

ing two limits. First, the second harmonic vanishes in the limit $J_{\text{stag}} \rightarrow 0$ owing to the inversion symmetry. Second, it tends to decrease for the larger J_{stag} . This can be understood by the analogy between HHG of semiconductors and that of the present spin systems. Namely, the photon energy $\hbar\Omega$ at $\Omega = 0.02$ is much smaller than the spin gap Δ_I for a sufficiently large J_{stag} and thus nonlinear optical processes such as multi-photon absorption is necessary for generating magnetic excitations and spin dynamics. Such nonlinear dynamics becomes suppressed in systems with a large J_{stag} (i.e., a large spin gap) and therefore the height of the second harmonic spin current decreases in the large- J_{stag} region. We remark that the third harmonics also exhibits the similar behavior to the second one, but more nontrivial J_{stag} dependence can arise in the third harmonics as shown in the panels (b) and (d) of Fig. 5. In particular, there exist a clear double peak structure in the panel (d). The authors do not have simple interpretation for this complicated behavior yet.

In addition to the case of $\Omega \ll \Delta_I$, we have also studied the second- and third-harmonic spin currents at $\Omega \sim \Delta_I$. In this case, the intensity profiles of $|J_{\text{spin}}(2\Omega)|$ and $|J_{\text{spin}}(3\Omega)|$ in the $(b_0(e_0), J_{\text{stag}})$ plane are respectively similar to those of $|I_P(2\Omega)|$ and $|I_P(3\Omega)|$ in Fig. 3.

Now we discuss the typical field amplitude required in experimental observations, following the same criterion mentioned at the end of Sec. III. As shown in Fig. 4, the second harmonic spin current has about a 10% of the fundamental one at $b_0 = 0.1$, and thus we regard this amplitude as required. According to Table I, this field amplitude corresponds to $B_0 = 0.74$ T (3.7 T) for magnets of energy scale $J = 10$ K (50 K). From Table III, this magnetic field amplitude corresponds to the electric field amplitude $E_0 = 2.2$ MV/cm (11 MV/cm) and the energy flux $I = 0.29$ GW/cm² (1.5 GW/cm²). The required amplitude for the magnetostriction effect is the same as the above values. The concrete experimental setups will be discussed in Sec. VI.

V. MAGNETIZATION

We have discussed the harmonic generation and spin current so far by using Hamiltonian (1), in which the total magnetization is conserved. For completeness, in this section, we switch to another Hamiltonian (see Eq. (23) below), investigating the harmonic generation through nonlinear magnetization dynamics. The methods that we have developed in previous sections apply to this model.

A. Model and Formulation

The second Hamiltonian that we consider in this section is the anisotropic XY model:

$$\hat{H}_{\text{II}} = \hat{H}_{\text{XY}} = J \sum_{j=1}^L \left[(1 + \epsilon) \hat{S}_j^x \hat{S}_{j+1}^x + (1 - \epsilon) \hat{S}_j^y \hat{S}_{j+1}^y - \beta_u \hat{S}_j^z \right], \quad (23)$$

where ϵ quantifies intraplane anisotropy and the last term with $\beta_u = g\mu_B B_0$ represents the uniform Zeeman coupling due to an applied external magnetic flux B_0 . For $\epsilon \neq 0$, the total magnetization $\sum_j \hat{S}_j^z$ is not a conserved quantity, and the Hamiltonian (23) is useful to study dynamics of magnetization. The case of the strongest Ising anisotropy, i.e., $\epsilon = 1$ corresponds to the so-called transverse-field Ising model. There exist several quasi-one-dimensional magnets with strong Ising anisotropy, e.g., CoNb_2O_6 ⁹², $\text{BaCo}_2\text{V}_2\text{O}_8$ ^{93,94}, and $\text{SrCo}_2\text{V}_2\text{O}_8$ ⁹⁵.

We consider the laser-spin interaction by the ac Zeeman coupling to the laser magnetic field $B(t)$ along the S^z direction as we have done in Sec. II A. Note that we do not consider staggered effects in this section. Thus the coupling Hamiltonian is given by

$$\hat{H}_{\text{ext,II}}^Z(t) = -\beta(t) \sum_j \hat{S}_j^z \quad (24)$$

with $\beta(t) \equiv B(t)\eta_Z^u$.

The total magnetization

$$\hat{M} = \sum_j \hat{S}_j^z. \quad (25)$$

is the observable that we consider for $\hat{H}_{\text{II}} + \hat{H}_{\text{ext,II}}^Z(t)$. As is the case with the electric polarization, the magnetization becomes the source of electromagnetic radiation when varies in time. Thus we consider the radiation power

$$I_M(\omega) \propto |\omega^2 M(\omega)|^2, \quad (26)$$

and discuss its peak structure in the following. As we remarked for the electric polarization in Sec. II A, a constant shift of $M(t) = \langle \hat{M} \rangle_t$ does not change $I_M(\omega)$, and thus we may use $\Delta M(t) = M(t) - M_0$ with $M_0 = \langle \hat{M} \rangle_{t_{\text{ini}}}$.

We remark that the odd-order harmonics exist for generic choices of the parameters whereas the even-order ones appear only when $\beta_u \neq 0$. This is analogous to the HHG selection rule in semiconductors regarding the inversion that has been discussed in Sec. II. Note, however, that the selection rule for $I_M(\omega)$ does not follow from the inversion symmetry unlike the HHG in semiconductors⁹⁶ since the magnetization is even under the inversion. For the magnetization, the rule can be obtained by using spin rotations as follows. We consider the ideal situation where $\beta(t)$ involves many cycles and is approximately sinusoidal with period $T = 2\pi/\Omega$. For the special case of

$\beta_u = 0$, the total Hamiltonian $\hat{H}_{\text{II}} + \hat{H}_{\text{ext,II}}^Z(t)$ is invariant under a dynamical transformation given by $t \rightarrow t + T/2$ combined with the global π rotation around, e.g., the S^y axis. Since \hat{M} is odd under this transformation, we have $M(t + T/2) = -M(t)$, which implies that the even-order HHG is prohibited. In fact, we have $M(2n\Omega) \propto \int_0^T dt e^{i2n\Omega t} M(t) = \int_0^T dt e^{i2n\Omega t} [M(t) + M(t + T/2)]/2 = 0$ (see Appendix A for more detail). However, for $\beta_u \neq 0$, this dynamical symmetry is broken and the even-order HHG by magnetization is allowed even if the inversion symmetry is present.

The above result shows that the even-order HHG can be controlled by the static magnetic field β_u , and this is a close analogy to the SHG controlled by the electric current in semiconductors⁹⁷ and superconductors^{98,99}. We stress that this controllability applies to a wide class of spin systems as long as the dynamical symmetry exists in the absence of the static magnetic field.

B. Fermionization and BCS Hamiltonian

Our new model is also fermionized via the Jordan-Wigner transform. Through the Fourier transformation of the Jordan-Wigner fermion $\hat{d}_k \equiv L^{-1/2} \sum_{j=1}^L e^{-ikj} \hat{c}_j$, the Hamiltonian (23) and the coupling (24) are given by

$$\hat{H}_{\text{II}} = \sum_k \left[(J \cos k + \beta_u) \hat{d}_k^\dagger \hat{d}_k + i(J/2)\epsilon \sin k (\hat{d}_k^\dagger \hat{d}_{-k}^\dagger + \hat{d}_k \hat{d}_{-k}) \right], \quad (27)$$

$$\hat{H}_{\text{ext,II}}^Z(t) = \beta(t) \sum_k \hat{d}_k^\dagger \hat{d}_k. \quad (28)$$

For simplicity, we assume that L is even and focus on the subspace of the states with even fermion numbers. Correspondingly, we impose the anti-periodic boundary condition for the fermion and take $k = \pm\pi(m + 1/2)/L$ ($m = 0, 1, \dots, L - 1$)¹⁰⁰.

Equation (27) is the same as a BCS-type Hamiltonian for superconductors^{101,102}. It means that the HHG of the anisotropic spin chain (23) is analogous to that of superconducting systems with a static Cooper-pairing coupling $i\epsilon J \sin k/2$ (i.e., without the dynamics of condensed wave function such as the Higgs mode). Similarly to Eq. (11), we have the 2×2 form of the Hamiltonian (27) as

$$\hat{H}_{\text{II}} = \sum_{k>0} \phi_{\text{II},k}^\dagger H_{\text{II}}(k) \phi_{\text{II},k} \quad (29)$$

where $\phi_{\text{II},k} \equiv {}^t(\hat{d}_k, \hat{d}_{-k}^\dagger)$ and the 2×2 Hamiltonian matrix $H_{\text{II}}(k)$ is defined by

$$H_{\text{II}}(k) = (J \cos k + \beta_u) \sigma_z - J\epsilon \sin k \sigma_y. \quad (30)$$

To diagonalize Eq. (29), we perform a unitary (Bogoliubov) transformation. Namely, we introduce $\gamma_k = u_k \hat{d}_k -$

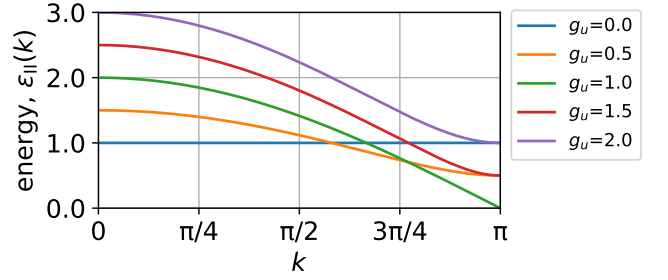


FIG. 6. Upper band $\epsilon_{\text{II}}(k)$ of the 2×2 matrix (33) for the transverse-field Ising chain ($\epsilon = 1$) in static Zeeman fields $g_u = 0.0, 0.5, \dots$, and 2.0. The energy unit is J and the lower band is given by $-\epsilon_{\text{II}}(k)$.

$v_k \hat{d}_{-k}^\dagger$ and $\gamma_{-k} = v_k \hat{d}_k^\dagger + u_k \hat{d}_{-k}$, where $u_k = \cos(\theta_k/2)$ and $v_k = i \sin(\theta_k/2)$ with $\tan \theta_k = -J\epsilon \sin k / (J \cos k + \beta_u)$, obtaining $\hat{H}_{\text{II}} = \sum_{k>0} \epsilon_{\text{II}}(k) (\hat{\gamma}_k^\dagger \hat{\gamma}_k + \hat{\gamma}_{-k}^\dagger \hat{\gamma}_{-k} - 1)$ with $\epsilon_{\text{II}}(k) = J \sqrt{(\cos k + g_u)^2 + (\epsilon \sin k)^2}$ and $g_u = \beta_u/J$. Thus, the ground state is the one annihilated by all the $\hat{\gamma}_{\pm k}$'s and written as¹⁰³

$$|\Psi_{\text{II}}\rangle = \prod_{k>0} (u_k + v_k \hat{d}_k^\dagger \hat{d}_{-k}^\dagger) |0\rangle, \quad (31)$$

where $|0\rangle$ being the Fock vacuum for the fermion $\{\hat{d}_k\}$.

Even under the ac Zeeman coupling (28), the time evolution of each k -subspace occurs within a two-dimensional space rather than the entire four-dimensional space. This is because the coupling conserves the number of the Jordan-Wigner (d) fermions and a single quasiparticle (γ) excitation is prohibited. We let $\hat{d}_k^\dagger \hat{d}_{-k}^\dagger |0_k\rangle$ and $|0_k\rangle$ ($|0_k\rangle$ is the Fock vacuum for the k -subspace) be the basis then the 2×2 -matrix representation of \hat{H}_{II} is given by Eq. (30) whose eigenstates are $|\psi_g(k)\rangle = {}^t(v_k, u_k)$ and $|\psi_e(k)\rangle = {}^t(u_k, v_k)$. The two eigenenergies $\pm \epsilon_{\text{II}}(k)$ define the two energy bands.

In the following, we focus on $\epsilon = 1$ corresponding to the transverse-field Ising model and assume $\beta_u > 0$. The energy bands are illustrated in Fig. 6. Then the energy gap, i.e., the minimum energy difference between the upper and lower bands, occurs at $k = \pi$ and is given by

$$\Delta_{\text{II}} = 2J|1 - g_u|. \quad (32)$$

In terms of the original spin model, $g_u = 1$ corresponds to the quantum critical point between the Néel ($0 < g_u < 1$) and the forced ferromagnetic ($g_u > 1$) phases^{86,100}.

Since our problem is two-dimensional in the above sense, we can use the quantum master equation (20) to analyze the dynamics with relaxation. In the present case, the Hamiltonian part corresponds to

$$H(k, t) = H_{\text{II}}(k) + \beta(t) \sigma_z. \quad (33)$$

and the Lindblad operator is $L_k = |\psi_g(k)\rangle \langle \psi_e(k)|$. The master equation is solved for the density matrix with the

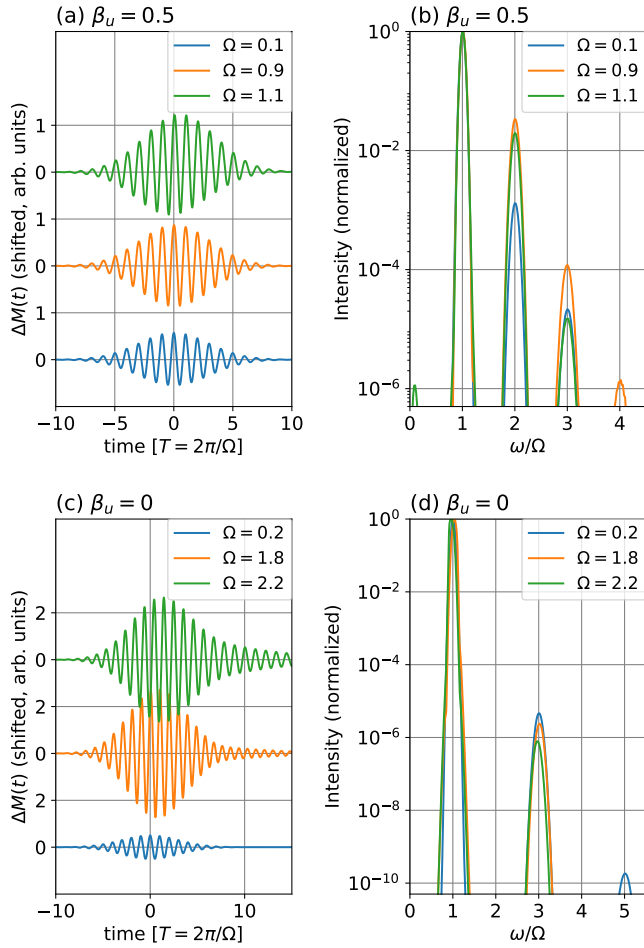


FIG. 7. (left) Time profile of $\Delta M(t)$ in the transverse-field Ising chain ($\epsilon = 1$) with the ac Zeeman driving $\hat{H}_{\text{ext,II}}^Z(t)$ at frequencies well below, slightly below and above the spin gap. The static Zeeman field is $\beta_u = 0.5$ (top) and $\beta_u = 0$ (bottom), where the spin gap is $\Delta_{\text{II}} = 1$ and 2 , respectively. The other parameters are $\beta_0 = 0.1$ and $\gamma = 0.1$. (right) Corresponding power spectrum $I_M(\omega)$ (7) plotted against ω/Ω for $\beta_u = 0.5$ (top) and $\beta_u = 0$ (bottom).

initial condition $\rho(k, t_{\text{ini}}) = |\psi_g(k)\rangle \langle \psi_g(k)|$. We set the driving field as a pulse shape

$$\beta(t) = \beta_0 \cos(\Omega t) f(t), \quad (34)$$

where β_0 is the peak coupling energy and $f(t)$ is the same as that in Sec. II A.

C. Numerical Results

Figure 7(a) shows a typical magnetization profiles in which we apply a laser pulse of Eq. (34) to the transverse-field Ising model. Here $g_u = 0.5$, i.e., $\Delta_{\text{II}} = 1$, and the driving frequencies are much smaller than or close to the gap. Their normalized power spectrum $I_M(\omega)$ is shown

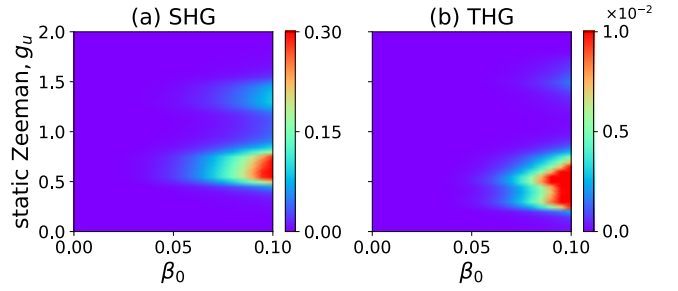


FIG. 8. Intensities of SHG [$I_M(2\Omega)$] (left) and THG [$I_M(3\Omega)$] (right) generated by ac-Zeeman-coupling driven magnetization dynamics in the transverse-field Ising chain ($\epsilon = 1$). The unit of intensity is chosen as $I_M(\Omega)$ at $\beta_0 = 0.05$ and $g_u = 0.5$. The other parameters are set as $\gamma = 0.1$ and $\Omega = 0.5$.

in Fig. 7(b). The even-order harmonics are present since $g_u \neq 0$ while we have confirmed that they are negligibly small in the absence of the static magnetic field, $g_u = 0$, as shown in Fig. 7(d). This is consistent with the symmetry argument in Sec. V A. Namely, we have numerically shown that the SHG is controllable by the static magnetic field.

Whereas the SHG is strong both for Ω slightly above and below the spin gap, the THG is stronger for Ω below the spin gap. Similarly to the electric polarization and the spin current discussed in the previous sections, the harmonic peaks remain narrow even for $\Omega \sim \Delta_{\text{II}}$ because of relaxation. Without relaxation, near-resonant driving causes strong real excitations, which destroy the clear peak structures. The interplay between the strong driving and relaxation results in the strong and clear THG signals.

We now systematically investigate the intensity of the HHG derived from magnetization dynamics. Figure 8 shows $I_M(2\Omega)$ and $I_M(3\Omega)$ in the (β_0, g_u) -plane with $\Omega = 0.5$, where the unit of intensity is taken as $I_M(\Omega)$ for $\beta_0 = 0.05$. This value of Ω corresponds to 0.10 THz (0.52 THz) for $J = 10$ K (50 K). Within the range of parameters in Fig. 8, the SHG (THG) intensity tends to monotonically increase with the ac Zeeman coupling β_0 and becomes as large as 30% (1%) of our reference fundamental harmonic.

The SHG and THG show nonmonotonic behaviors in the static magnetic field g_u . These behaviors are understood by the multi-photon processes in a perturbative viewpoint as follows. As g_u increases from 0, the spin gap Δ_{II} decreases according to Eq. (32) (see also Fig. 6). When the gap becomes smaller than 3Ω (2Ω), the three-(two-)photon process becomes significant and the THG (SHG) starts to increase. One might expect that the THG (SHG) enhances resonantly when the resonance condition 3Ω (2Ω) = $\Delta_{\text{II}} = 2\epsilon_{\text{II}}(k = \pi)$ is satisfied, but this enhancement is not observed in Fig. 8. This is because the resonance occurs at $k = \pi$, but the ac Zeeman coupling at $k = \pi$ has no matrix elements between

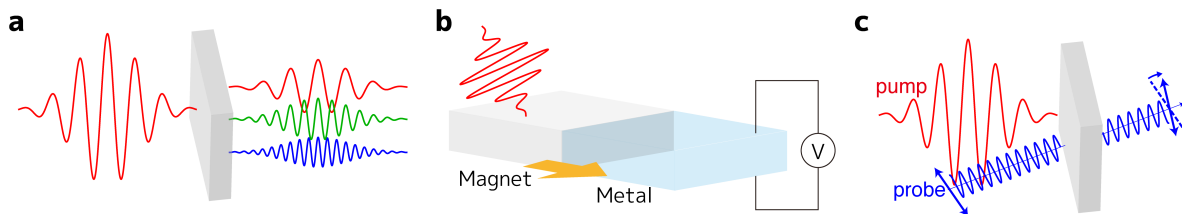


FIG. 9. Schematic illustrations of experimental setups to observe harmonic generation and spin currents. (a) Strong THz laser induces nonlinear oscillations of the electric polarization or the magnetization, which gives rise to harmonic generation. (b) Harmonic spin currents induced by strong THz waves in a magnet sample are injected into an attached metal, where the electromotive force is induced by the inverse spin Hall effect. (c) An all-optical setup to detect harmonic spin currents generated by strong GHz pumps. The spin currents are detected by a weak probe high-frequency wave, whose polarization changes according to the Faraday rotation.

the upper and lower bands [see Eqs. (33) and (30)]. As g_u increases further to approach the quantum critical point $g_u = 1$ and the spin gap vanishes, the SHG and THG decrease. This is because near $g_u = 1$ the band dispersion $\epsilon_{II}(k)$ becomes like a Dirac cone and the density of state decreases. As g_u increases from unity, the spin gap grows again and the SHG and THG increase. However, the HHG finally decreases to almost vanish when the gap becomes larger than 2Ω and 3Ω and the multi-photon processes are not significant.

Figure 8 clearly shows that the SHG and THG are generally smaller in the forced ferromagnetic phase ($g_u > 1$) than in the Néel one ($0 < g_u < 1$). This would be understood from the value of the magnetization along the S^z direction. Namely, the initial magnetization M_0 becomes larger with increase of g_u , and thus the application of the ac Zeeman field along the same direction leads to less-efficient magnetization oscillations.

Let us estimate the required field amplitude to observe the HHG through magnetization in our model. We again follow the criterion discussed at the end of Sec. III, and regard $\beta_0 = 0.1$ as the required amplitude from the $\Omega \sim 1$ data in Fig. 7. This pair of β_0 and Ω corresponds to $B_0 = 0.74$ T at 0.21 THz for magnets of energy scale $J = 10$ K and $B_0 = 3.7$ T at 1.0 THz for those of $J = 50$ K. Compared to the HHG through the electric polarization discussed in Sec. III, this amplitude is one-order more demanding. This might be related to the difference between the origins of the SHG. While we considered an inversion-asymmetric model in Sec. III, we here discuss another one with broken dynamical symmetry regarding spin rotations. The HHG by magnetization in inversion-asymmetric models would merit future study.

VI. EXPERIMENTAL PROTOCOLS

We have shown that harmonic responses can be generated in spin systems by THz and GHz electromagnetic waves. In this section, we propose some ways to observe them, and discuss how intense electromagnetic waves are

required.

To detect the harmonic generation through the electric polarization and the magnetization, it is useful to observe the radiation from them by a spectrometer as shown in Fig. 9(a). This is basically the same as that of HHG in semiconductors.

On top of detecting the radiation, the harmonic spin currents could be detected by the following two methods. The first one is based on electric technology and attaching a spin-orbit-coupled metal on the sample magnetic insulator as shown in Fig. 9(b). In this method, the generated ac spin currents are injected into the metal. Then these spin currents are converted into the ac electric currents through the inverse spin Hall effect^{104–106}. Finally these electric currents are detected as the ac electric voltage if the frequency is sufficiently low. As we already mentioned, high frequency electric voltage cannot be detected by the standard electric method and thus the frequency of the applied laser field should be equivalent to or smaller than several tens of THz⁹¹. The second one is an all-optical pump-probe method as shown in Fig. 9(c). In this method, a weak high-frequency, e.g., visible light wave detects the magnetization dynamics driven by GHz or THz pump waves through the Kerr effect or the Faraday rotation.

VII. EXTREMELY STRONG FIELDS

We have been focusing mainly on the second and third harmonics and the required field strengths to observe them. We have shown that these harmonics could be observable with the state-of-the-art intense lasers even though the laser-spin coupling is weak in principle. Meanwhile, it is still of theoretical interest to investigate even higher-order harmonics generated by extremely strong lasers that would not be available in the current technology. In particular, since our spin models correspond to electron systems such as semiconductors and superconductors, this investigation leads to extending the correspondence of the models to that of the HHG spectra.

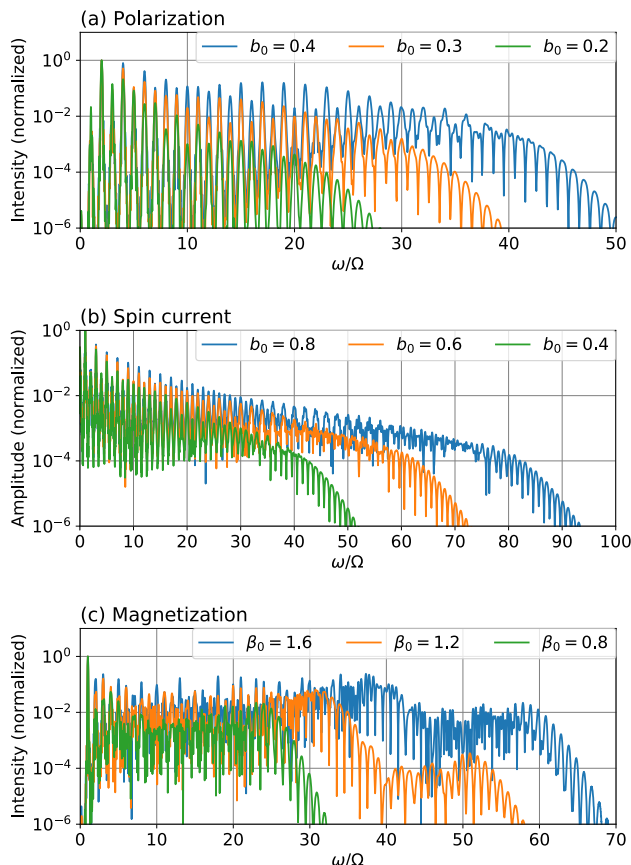


FIG. 10. (a) Power spectrum $I_P(\omega)$ (7) for extremely strong Zeeman drivings $\hat{H}_{\text{ext}}^Z(t)$ with $b_0 = 0.2, 0.3,$ and 0.4 . (b) Amplitude spectrum $|J_{\text{spin}}(\omega)|$ for extremely strong Zeeman drivings $\hat{H}_{\text{ext}}^Z(t)$ with $b_0 = 0.4, 0.6,$ and 0.8 . In both (a) and (b), the Hamiltonian is \hat{H}_I with $J_{\text{stag}} = 0.1$ and $H_{\text{stag}} = 0.03$, where the spin gap is $\Delta_I = 0.21$, and the driving frequency of $\hat{H}_{\text{ext}}^Z(t)$ is well-below the gap $\Omega = 0.02$. Also, the data are normalized so that the highest peak is unity for each spectrum. (c) Power spectrum $I_M(\omega)$ in the transverse-field Ising chain ($\epsilon = 1$) for extremely strong drivings with $\beta_0 = 0.8, 1.2,$ and 1.6 . The parameters are $\beta_u = 0.5$ where the spin gap is $\Delta_{II} = 1.0$ and the driving frequency is well-below the gap $\Omega = 0.1$. The data are normalized so that the highest peak is unity for each spectrum.

Let us first consider the HHG spectra by the polarization (7) in the model introduced in Sec. II. As we remarked in Sec. II, our spin model in the fermion language is analogous to the semiconductors. Thus, if a very strong field is applied, our spin system is expected to give HHG spectra similar to those of the semiconductors. This is indeed the case as shown in Fig. 10(a), in which we show the power spectrum $I_P(\omega)$ (7) for the Zeeman driving for example. Note that the field amplitude b_0 is more than 10 times larger than those used in Sec. III. We clearly see the plateau structure followed by the rapid decrease of intensity. The harmonic order at

which the rapid decrease sets in is known as the cutoff order in the semiconductor HHG⁴, which is roughly read from Fig. 10(a) as 20, 30, and 40 for $b_0 = 0.2, 0.3,$ and 0.4 , respectively. This linear scaling of the cutoff order to the field amplitude is known as a unique feature of the semiconductor HHG. Therefore, the similarity of our spin system to the semiconductor system extends to that of HHG spectra in these two systems.

A similar correspondence to the semiconductor HHG is seen in the spin-current spectrum $|J_{\text{spin}}(\omega)|$ as well. Figure 10(b) shows the results for extremely strong Zeeman fields with $b_0 = 0.4, 0.6,$ and 0.8 . (see figure caption for the other parameters). For, e.g., $b_0 = 0$, we observe that the harmonic peak slowly decreases upto $\omega/\Omega \lesssim 80$ and then rapidly decays. We interpret this as an approximate plateau with cutoff order about 80. The cutoff order thus defined is read out as ~ 60 and ~ 40 for $b_0 = 0.6$ and 0.4 , respectively. Thus the cutoff order roughly scales linearly with b_0 in line with the semiconductor HHG.

Finally we investigate the HHG spectra by the magnetization (26) for the transverse-field Ising chain ($\epsilon = 1$). As remarked in Sec. V, this model is mapped to a BCS-type model of superconductors. Figure 10(c) shows $I_M(\omega)$ for $\beta_0 = 0.8, 1.2,$ and 1.6 that are roughly 10 times larger than those we have considered in Sec. V. For $\beta_0 = 0.8$ we observe a plateau-like behavior upto $\omega/\Omega \lesssim 25$ and then a rapid decrease. The width of the plateau-like behavior increases almost linearly, roughly speaking, with the field amplitude β_0 . It is more remarkable that the second plateau emerges for higher fields and observed for $\beta_0 = 1.2$ and 1.6 . The second plateau has not been seen in Figs. 10(a) and (b), for which the Hamiltonian is analogous to semiconductors. Thus the second plateau might possibly related to superconductors, to which the present model is analogous. We leave further study on this relation as a future work.

VIII. CONCLUSIONS

We have investigated the harmonic generation and harmonic spin currents in magnetic insulators. To this end, we have considered simple but realistic models of quantum spin chains and studied the laser-driven nonlinear dynamics by means of the quantum master equation. In Sec. II, we have introduced the inversion-asymmetric spin chain to study the HHG by electric polarization and spin current. Through the Jordan-Wigner transformation, the model is exactly mapped to a two-band fermion model like semiconductors. We have confirmed that both intra- and inter-band transitions of the Jordan-Wigner fermions are relevant to generate harmonic peaks similarly to the HHG of semiconductors. On the other hand, we have focused on the transverse-field Ising chain to explore HHG by magnetization dynamics in Sec. V, and the chain is mapped to a fermion model with a BCS-type Hamiltonian. Calculating the quantum dynamics under pulse lasers and relaxation in Secs. III-V, we have shown

that the harmonic peaks can appear in the electric polarization, the spin current, and the magnetization. As shown in Figs. 2, 4, and 7, these harmonic peaks have been obtained in a well-defined manner thanks to the relaxation taken in our quantum master equation. For hypothetical strong fields, we have obtained the harmonic spectra involving plateaus in our spin models and pointed out the correspondence to the spectra in semiconductors and superconductors (see Fig. 10).

For realistic field strength within the state-of-the-art technology, the obtained harmonics become large enough to be experimentally observed. The required ac electric-field strength is typically $E_0 = 100 \text{ kV/cm} \sim 1 \text{ MV/cm}$. The THz and GHz waves with these field strengths could be achieved within the current laser technology^{40–43}. The data in Tables I–III would be useful to semi-quantitatively estimate the required laser field to experimentally create HHG in magnets. We have shown that the harmonic peaks are not sensitive to the driving frequency and the field strength is more important for a successful detection. It is noteworthy that the SHG from magnetization dynamics has been shown controllable by static Zeeman fields. This controllability applies to a wide class of magnetic insulators.

We have proposed some experimental ways of observing HHG in magnetic insulators in Sec. VI. In addition to the optical method, we have considered electric ways of detecting high-harmonic spin currents (see Fig. 9). An intense GHz wave (i.e., sufficiently low-frequency laser or electromagnetic wave) is necessary to use the electric methods.

As we mentioned in Introduction, the HHG is a typical and simple nonlinear optical phenomenon in solids. Therefore, our estimate for the required ac field strength ($E_0 = 100 \text{ kV/cm} \sim 1 \text{ MV/cm}$) would serve as a reference value not only for future HHG experiments in real magnets but also for other nonlinear magneto-optical effects such as Floquet engineering of magnetism^{53,54}, dc spin current rectification with THz or GHz waves^{62,63}, inverse Faraday effects^{51,52}, etc.

Extensions of the present work to magnonic systems are future work of interest. A difference from our present model mappable to the Jordan-Wigner fermions is that the magnons may exhibit resonances to the external field and stronger signals could be obtained in certain conditions. Of course, more quantitative theoretical evaluations specific to each material become important when one interprets concrete experiments.

ACKNOWLEDGEMENTS

Fruitful discussions with Hiroaki Ishizuka, Daichi Hirobe, and Masashi Fujisawa are gratefully acknowledged. T.N.I. is supported by JSPS KAKENHI Grant No. JP18K13495. M.S. is supported by JSPS KAKENHI Grant No. 17K05513 and a Grant-in-Aid for Scientific Research on Innovative Areas “Quantum Liquid Crys-

tals” (Grant No. JP19H05825).

Appendix A: HHG selection rule for magnetization dynamics

We supplement the argument in Sec. V A, where the even-order harmonics are shown to vanish when the static Zeeman field is absent $\beta_u = 0$. The key equation is

$$M(t) = -M(t + T/2), \quad (\text{A1})$$

which is satisfied by the time-dependent expectation value of the total magnetization. In this appendix, we derive the above equation by more careful calculations.

For simplicity, we restrict ourselves to the Ising case $\epsilon = 1$. In this case, both the static Hamiltonian \hat{H}_{XY} and the ground state are invariant under the global π rotation around the S^x axis $\hat{U}_\pi^x, \hat{U}_\pi^x \hat{S}_j^\alpha \hat{U}_\pi^{x\dagger} = -\hat{S}_j^\alpha$ ($\alpha = y, z$) and $\hat{U}_\pi^x \hat{S}_j^x \hat{U}_\pi^{x\dagger} = \hat{S}_j^x$. Note that our argument can easily be generalized to the general case $\epsilon \neq 1$, where the symmetry axis depends on ϵ .

Let us express the symmetry in terms of the Jordan-Wigner fermions. As one can check easily, The global rotation \hat{U}_π^x leads to $\hat{U}_\pi^x \hat{c}_j \hat{U}_\pi^{x\dagger} = (-1)^j \hat{c}_j^\dagger$, which implies, in the Fourier transform, that $\hat{U}_\pi^x \hat{d}_k \hat{U}_\pi^{x\dagger} = \hat{d}_{\pi-k}^\dagger$. Then the rotational invariance of \hat{H}_{XY} is translated into the 2×2 -matrix representation (33) as

$$H_{\text{II}}(\pi - k) = \sigma_y H_{\text{II}}(k) \sigma_y \quad (\text{A2})$$

for $\beta_u = 0$. This means that there is one-to-one correspondence between the energy eigenstates of $H_{\text{II}}(\pi - k)$ and $H_{\text{II}}(k)$, which leads to

$$\rho(\pi - k, t_{\text{ini}}) = \sigma_y \rho(k, t_{\text{ini}}) \sigma_y. \quad (\text{A3})$$

at the initial time.

Next, we consider the dynamical symmetry, supposing the multi-cycle limit, at which $T/t_{\text{FWHM}} \gg 1$ and $\beta(t)$ is approximately sinusoidal. In this situation, the ac Zeeman field satisfies $\beta(t + T/2) = -\beta(t)$, and the total Hamiltonian $\hat{H}(t) = \hat{H}_{\text{II}} + \hat{H}_{\text{ext,II}}^Z(t)$ has the dynamical symmetry $\hat{H}(t) = \hat{U}_\pi^x \hat{H}(t + T/2) \hat{U}_\pi^{x\dagger}$. In the fermion language, this dynamical symmetry reads

$$H(\pi - k, t) = \sigma_y H(k, t + T/2) \sigma_y. \quad (\text{A4})$$

We remark that the Lindblad operators satisfy similar relations

$$L_{\pi-k} = e^{i\varphi_k} \sigma_y L_k \sigma_y, \quad (\text{A5})$$

where φ_k is some real number.

Equations (A4) and (A5) relate the dynamics of $\rho(k, t)$ and $\rho(\pi - k, t)$. To see this, we symbolically represent the quantum master equation (20) by using the Liouvillian super operator

$$\frac{d}{dt} \rho(k, t) = \mathcal{L}_k(t) \rho(k, t). \quad (\text{A6})$$

Equations (A4) and (A5) lead to

$$\begin{aligned} \frac{d}{dt}\rho(\pi - k, t) &= \mathcal{L}_{\pi-k}(t)\rho(\pi - k, t) \\ &= \sigma_y \mathcal{L}_k(t + T/2)\sigma_y \rho(\pi - k, t), \end{aligned} \quad (\text{A7})$$

and thus to

$$\frac{d}{dt}\sigma_y \rho(\pi - k, t)\sigma_y = \mathcal{L}_k(t + T/2)\sigma_y \rho(\pi - k, t)\sigma_y. \quad (\text{A8})$$

Comparing Eqs. (A6) and (A8), we obtain

$$\sigma_y \rho(\pi - k, t)\sigma_y = \rho(k, t + T/2) \quad (\text{A9})$$

if $\sigma_y \rho(\pi - k, t_{\text{ini}})\sigma_y = \rho(k, t_{\text{ini}} + T/2)$. This condition is actually satisfied because of the following reasons. First, Eq. (A3) holds true. Second, the time evolution of $\rho(k, t)$ from $t = t_{\text{ini}}$ to $t_{\text{ini}} + T/2$ is negligible because we have taken such a small t_{ini} that the ac Zeeman field is negligible at $t \sim t_{\text{ini}}$.

Finally, we discuss the magnetization, which is given in the 2×2 -matrix representation by

$$M_k = -\sigma_z \quad (\text{A10})$$

independently of k . Thus, Eq. (A9) leads to the following relations for the expectation values of magnetization:

$$\begin{aligned} M(\pi - k, t) &= \text{tr}[(-\sigma_z)\rho(\pi - k, t)] \\ &= \text{tr}[(-\sigma_z)\sigma_y \rho(k, t + T/2)\sigma_y] \\ &= -\text{tr}[(-\sigma_z)\rho(k, t + T/2)] \\ &= -M(k, t + T/2), \end{aligned} \quad (\text{A11})$$

where we have used the cyclic property of the trace and $\sigma_y \sigma_z \sigma_y = -\sigma_z$. Therefore, the total magnetization $M(t)$ satisfies

$$\begin{aligned} M(t) &= \sum_k M(k, t) \\ &= \sum_k M(\pi - k, t + T/2) \\ &= -M(t + T/2). \end{aligned} \quad (\text{A12})$$

Thus we have obtained Eq. (A1).

-
- ¹ F. Calegari, G. Sansone, S. Stagira, C. Vozzi, and M. Nisoli, *Journal of Physics B: Atomic, Molecular and Optical Physics* **49**, 062001 (2016).
- ² T. Brabec and F. Krausz, *Reviews of Modern Physics* **72**, 545 (2000).
- ³ S. Ghimire, A. D. DiChiara, E. Sistrunk, P. Agostini, L. F. DiMauro, and D. A. Reis, *Nature Physics* **7**, 138 (2011).
- ⁴ S. Ghimire, G. Ndabashimiye, A. D. DiChiara, E. Sistrunk, M. I. Stockman, P. Agostini, L. F. DiMauro, and D. A. Reis, *Journal of Physics B: Atomic, Molecular and Optical Physics* **47**, 204030 (2014).
- ⁵ O. Schubert, M. Hohenleutner, F. Langer, B. Urbanek, C. Lange, U. Huttner, D. Golde, T. Meier, M. Kira, S. W. Koch, and R. Huber, *Nature Photonics* **8**, 119 (2014).
- ⁶ M. Hohenleutner, F. Langer, O. Schubert, M. Knorr, U. Huttner, S. W. Koch, M. Kira, and R. Huber, *Nature* **523**, 572 (2015).
- ⁷ T. T. Luu, M. Garg, S. Y. Kruchinin, A. Moulet, M. T. Hassan, and E. Goulielmakis, *Nature* **521**, 498 (2015).
- ⁸ G. Ndabashimiye, S. Ghimire, M. Wu, D. A. Browne, K. J. Schafer, M. B. Gaarde, and D. A. Reis, *Nature* **534**, 520 (2016).
- ⁹ G. Vampa, B. G. Ghamsari, S. Siadat Mousavi, T. J. Hammond, A. Olivieri, E. Lisicka-Skrek, A. Y. Naumov, D. M. Villeneuve, A. Staudte, P. Berini, and P. B. Corkum, *Nature Physics* **13**, 659 (2017).
- ¹⁰ K. Kaneshima, Y. Shinohara, K. Takeuchi, N. Ishii, K. Imasaka, T. Kaji, S. Ashihara, K. L. Ishikawa, and J. Itatani, *Physical Review Letters* **120**, 243903 (2018).
- ¹¹ F. H. M. Faisal and R. Genieser, *Physics Letters A* **141**, 297 (1989).
- ¹² M. Holthaus and D. W. Hone, *Phys. Rev. B* **49**, 16605 (1994).
- ¹³ D. Golde, T. Meier, and S. W. Koch, *Journal of the Optical Society of America B* **23**, 2559 (2006).
- ¹⁴ D. Golde, T. Meier, and S. W. Koch, *Physical Review B* **77**, 075330 (2008).
- ¹⁵ M. Korbman, S. Yu Kruchinin, and V. S. Yakovlev, *New Journal of Physics* **15**, 013006 (2013).
- ¹⁶ G. Vampa, C. R. McDonald, G. Orlando, P. B. Corkum, and T. Brabec, *Physical Review B* **91**, 064302 (2015).
- ¹⁷ M. Wu, S. Ghimire, D. A. Reis, K. J. Schafer, and M. B. Gaarde, *Physical Review A* **91**, 043839 (2015).
- ¹⁸ T. Ikemachi, Y. Shinohara, T. Sato, J. Yumoto, M. Kuwata-Gonokami, and K. L. Ishikawa, *Physical Review A* **95**, 043416 (2017).
- ¹⁹ T. N. Ikeda, *Physical Review A* **97**, 063413 (2018).
- ²⁰ C. L. Xia, Q. Q. Li, H. F. Cui, C. P. Zhang, and X. Y. Miao, *Europhysics Letters* **125**, 24004 (2019).
- ²¹ F. Navarrete, M. F. Ciappina, and U. Thumm, *Physical Review A* **100**, 33405 (2019).
- ²² S. A. Mikhailov and K. Ziegler, *Journal of Physics: Condensed Matter* **20**, 384204 (2008).
- ²³ N. Yoshikawa, T. Tamaya, and K. Tanaka, *Science (New York, N.Y.)* **356**, 736 (2017).
- ²⁴ H. A. Hafez, S. Kovalev, J.-C. Deinert, Z. Mics, B. Green, N. Awari, M. Chen, S. Germanskiy, U. Lehnert, J. Teichert, Z. Wang, K.-J. Tielrooij, Z. Liu, Z. Chen, A. Narita, K. Müllen, M. Bonn, M. Gensch, and D. Turchinovich, *Nature* **561**, 507 (2018).
- ²⁵ B. Cheng, N. Kanda, T. N. Ikeda, T. Matsuda, P. Xia, T. Schumann, S. Stemmer, J. Itatani, N. P. Armitage, and R. Matsunaga, (2019), arXiv:1908.07164.
- ²⁶ R. Matsunaga, N. Tsuji, H. Fujita, A. Sugioka, K. Makise, Y. Uzawa, H. Terai, Z. Wang, H. Aoki, and R. Shimano, *Science* **345**, 1145 (2014).

- ²⁷ Y. Kawakami, T. Amano, Y. Yoneyama, Y. Akamine, H. Itoh, G. Kawaguchi, H. M. Yamamoto, H. Kishida, K. Itoh, T. Sasaki, S. Ishihara, Y. Tanaka, K. Yonemitsu, and S. Iwai, *Nature Photonics* **12**, 474 (2018).
- ²⁸ K. Yonemitsu, *Journal of the Physical Society of Japan* **87**, 124703 (2018).
- ²⁹ T. Nag, R.-J. Slager, T. Higuchi, and T. Oka, arXiv:1802.02161 (2018).
- ³⁰ T. N. Ikeda, K. Chinzei, and H. Tsunetsugu, *Physical Review A* **98**, 063426 (2018).
- ³¹ Y. Murakami, M. Eckstein, and P. Werner, *Physical Review Letters* **121**, 057405 (2018).
- ³² Y. Murakami and P. Werner, *Physical Review B* **98**, 075102 (2018).
- ³³ S. Imai, A. Ono, and S. Ishihara, (2019), arXiv:1907.05687.
- ³⁴ D. Bauer and K. K. Hansen, *Physical Review Letters* **120**, 177401 (2018).
- ³⁵ C. Jürß and D. Bauer, *Phys. Rev. B* **99**, 195428 (2019).
- ³⁶ Y. S. You, Y. Yin, Y. Wu, A. Chew, X. Ren, F. Zhuang, S. Gholam-Mirzaei, M. Chini, Z. Chang, and S. Ghimire, *Nature Communications* **8**, 724 (2017).
- ³⁷ P. Jürgens, B. Liewehr, B. Kruse, C. Peltz, D. Engel, A. Husakou, T. Witting, M. Ivanov, M. J. J. Vrakking, T. Fennel, and A. Mermillod-Blondin, arXiv:1905.05126 (2019).
- ³⁸ K. Chinzei and T. N. Ikeda, arXiv:1905.05205.
- ³⁹ A. Kirilyuk, A. V. Kimel, and T. Rasing, *Reviews of Modern Physics* **82**, 2731 (2010).
- ⁴⁰ H. Hirori, A. Doi, F. Blanchard, and K. Tanaka, *Applied Physics Letters* **98**, 91106 (2011).
- ⁴¹ S. S. Dhillon, M. S. Vitiello, E. H. Linfield, A. G. Davies, M. C. Hoffmann, J. Booske, C. Paoloni, M. Gensch, P. Weightman, G. P. Williams, E. Castro-Camus, D. R. S. Cumming, F. Simoens, I. Escorcia-Carranza, J. Grant, S. Lucyszyn, M. Kuwata-Gonokami, K. Konishi, M. Koch, C. A. Schmuttenmaer, T. L. Cocker, R. Huber, A. G. Markelz, Z. D. Taylor, V. P. Wallace, J. A. Zeitler, J. Sibik, T. M. Korter, B. Ellison, S. Rea, P. Goldsmith, K. B. Cooper, R. Appleby, D. Pardo, P. G. Huggard, V. Krozer, H. Shams, M. Fice, C. Renaud, A. Seeds, A. Stöhr, M. Naftaly, N. Ridler, R. Clarke, J. E. Cunningham, and M. B. Johnston, *Journal of Physics D: Applied Physics* **50**, 43001 (2017).
- ⁴² B. Liu, H. Bromberger, A. Cartella, T. Gebert, M. Först, and A. Cavalleri, *Opt. Lett.* **42**, 129 (2017).
- ⁴³ Y. Mukai, H. Hirori, T. Yamamoto, H. Kageyama, and K. Tanaka, *New Journal of Physics* **18**, 13045 (2016).
- ⁴⁴ J. Lu, X. Li, H. Y. Hwang, B. K. Ofori-Okai, T. Kurihara, T. Suemoto, and K. A. Nelson, *Phys. Rev. Lett.* **118**, 207204 (2017).
- ⁴⁵ K. Yamaguchi, M. Nakajima, and T. Suemoto, *Physical Review Letters* **105**, 237201 (2010).
- ⁴⁶ A. Pimenov, A. A. Mukhin, V. Y. Ivanov, V. D. Travkin, A. M. Balbashov, and A. Loidl, *Nature Physics* **2**, 97 (2006).
- ⁴⁷ Y. Takahashi, R. Shimano, Y. Kaneko, H. Murakawa, and Y. Tokura, *Nature Physics* **8**, 121 (2011).
- ⁴⁸ T. Kubacka, J. A. Johnson, M. C. Hoffmann, C. Vicario, S. de Jong, P. Beaud, S. Gröbel, S.-W. Huang, L. Huber, L. Patthey, Y.-D. Chuang, J. J. Turner, G. L. Dakovski, W.-S. Lee, M. P. Minitti, W. Schlotter, R. G. Moore, C. P. Hauri, S. M. Koohpayeh, V. Scagnoli, G. Ingold, S. L. Johnson, and U. Staub, *Science* **343**, 1333 (2014).
- ⁴⁹ S. Baierl, M. Hohenleutner, T. Kampfrath, A. K. Zvezdin, A. V. Kimel, R. Huber, and R. V. Mikhaylovskiy, *Nature Photonics* **10**, 715 (2016).
- ⁵⁰ A. A. Sirenko, P. Marsik, C. Bernhard, T. N. Stanislavchuk, V. Kiryukhin, and S.-W. Cheong, *Phys. Rev. Lett.* **122**, 237401 (2019).
- ⁵¹ S. Takayoshi, H. Aoki, and T. Oka, *Physical Review B* **90**, 085150 (2014), arXiv:1302.4460.
- ⁵² S. Takayoshi, M. Sato, and T. Oka, *Physical Review B* **90**, 214413 (2014), arXiv:1402.0881.
- ⁵³ M. Sato, S. Takayoshi, and T. Oka, *Physical Review Letters* **117**, 147202 (2016), arXiv:1602.03702.
- ⁵⁴ M. Sato, Y. Sasaki, and T. Oka, (2014), arXiv:1404.2010.
- ⁵⁵ H. Fujita and M. Sato, *Phys. Rev. B* **95**, 54421 (2017).
- ⁵⁶ H. Fujita and M. Sato, *Phys. Rev. B* **96**, 60407 (2017).
- ⁵⁷ H. Fujita and M. Sato, *Scientific Reports* **8**, 15738 (2018).
- ⁵⁸ H. Fujita, Y. Tada, and M. Sato, *New Journal of Physics* **21**, 73010 (2019).
- ⁵⁹ J. H. Mentink, K. Balzer, and M. Eckstein, *Nature Communications* **6**, 1 (2015).
- ⁶⁰ K. Takasan and M. Sato, *Physical Review B* **100**, 60408 (2019).
- ⁶¹ M. Mochizuki and N. Nagaosa, *Phys. Rev. Lett.* **105**, 147202 (2010).
- ⁶² H. Ishizuka and M. Sato, *Phys. Rev. Lett.* **122**, 197702 (2019).
- ⁶³ H. Ishizuka and M. Sato, (2019), arXiv:1907.02734.
- ⁶⁴ S. Takayoshi, Y. Murakami, and P. Werner, *Phys. Rev. B* **99**, 184303 (2019).
- ⁶⁵ V. Kiryukhin, B. Keimer, J. P. Hill, and A. Vigliante, *Phys. Rev. Lett.* **76**, 4608 (1996).
- ⁶⁶ M. Arai, M. Fujita, M. Motokawa, J. Akimitsu, and S. M. Bennington, *Phys. Rev. Lett.* **77**, 3649 (1996).
- ⁶⁷ W. Palme, G. Àmbert, J.-P. Boucher, G. Dhahenne, and A. Revcolevschi, *J. Appt. Phys.* **79**, 5384 (1996).
- ⁶⁸ F. D. M. Haldane, *Phys. Rev. B* **25**, 4925 (1982).
- ⁶⁹ S. Takayoshi and M. Sato, *Phys. Rev. B* **82**, 214420 (2010).
- ⁷⁰ M. Sato, H. Katsura, and N. Nagaosa, *Phys. Rev. Lett.* **108**, 237401 (2012).
- ⁷¹ J. B. Torrance, J. E. Vazquez, J. J. Mayerle, and V. Y. Lee, *Phys. Rev. Lett.* **46**, 253 (1981).
- ⁷² N. Nagaosa and J.-i. Takimoto, *Journal of the Physical Society of Japan* **55**, 2735 (1986).
- ⁷³ H. Katsura, M. Sato, T. Furuta, and N. Nagaosa, *Phys. Rev. Lett.* **103**, 177402 (2009).
- ⁷⁴ M. Oshikawa and I. Affleck, *Phys. Rev. Lett.* **79**, 2883 (1997).
- ⁷⁵ I. Affleck and M. Oshikawa, *Phys. Rev. B* **60**, 1038 (1999).
- ⁷⁶ M. Sato and M. Oshikawa, *Phys. Rev. B* **69**, 54406 (2004).
- ⁷⁷ D. C. Dender, P. R. Hammar, D. H. Reich, C. Broholm, and G. Aeppli, *Phys. Rev. Lett.* **79**, 1750 (1997).
- ⁷⁸ R. Feyerherm, S. Abens, D. Günther, T. Ishida, M. Meißner, M. Meschke, T. Nogami, and M. Steiner, *Journal of Physics: Condensed Matter* **12**, 8495 (2000).
- ⁷⁹ R. Morisaki, T. Ono, H. Tanaka, and H. Nojiri, *Journal of the Physical Society of Japan* **76**, 63706 (2007).
- ⁸⁰ I. Umegaki, H. Tanaka, T. Ono, H. Uekusa, and H. Nojiri, *Phys. Rev. B* **79**, 184401 (2009).
- ⁸¹ K. Nawa, O. Janson, and Z. Hiroi, *Phys. Rev. B* **96**, 104429 (2017).
- ⁸² O. Masaki, U. Kazuo, A. Hidekazu, O. Akira, and K. Masahumi, *Journal of the Physical Society of Japan*

- 68, 3181 (1999).
- ⁸³ P. A. Franken, A. E. Hill, C. W. Peters, and G. Weinreich, *Physical Review Letters* **7**, 118 (1961).
- ⁸⁴ Y. Tokura, S. Seki, and N. Nagaosa, *Reports on Progress in Physics* **77**, 076501 (2014).
- ⁸⁵ R. W. Boyd, *Nonlinear Optics*, 3rd ed. (Academic Press, 2008).
- ⁸⁶ S. Sachdev, *Quantum Phase Transitions* (Cambridge University Press, 2011).
- ⁸⁷ H.-P. Breuer and F. Petruccione, *The Theory of Open Quantum Systems* (Oxford University Press, 2007).
- ⁸⁸ A. Pimenov, A. M. Shuvaev, A. A. Mukhin, and A. Loidl, *Journal of Physics: Condensed Matter* **20**, 434209 (2008).
- ⁸⁹ D. Hivonen, U. Nagel, T. Rööm, Y. J. Choi, C. L. Zhang, S. Park, and S.-W. Cheong, *Phys. Rev. B* **80**, 100402 (2009).
- ⁹⁰ S. Furukawa, M. Sato, and S. Onoda, *Phys. Rev. Lett.* **105**, 257205 (2010).
- ⁹¹ D. Wei, M. Obstbaum, M. Ribow, C. H. Back, and G. Woltersdorf, *Nature Communications* **5**, 3768 (2014).
- ⁹² R. Coldea, D. A. Tennant, E. M. Wheeler, E. Wawrzynska, D. Prabhakaran, M. Telling, K. Habicht, P. Smeibidl, and K. Kiefer, *Science* **327**, 177 (2010).
- ⁹³ S. Kimura, H. Yashiro, K. Okunishi, M. Hagiwara, Z. He, K. Kindo, T. Taniyama, and M. Itoh, *Physical Review Letters* **99**, 87602 (2007).
- ⁹⁴ S. Kimura, T. Takeuchi, K. Okunishi, M. Hagiwara, Z. He, K. Kindo, T. Taniyama, and M. Itoh, *Physical Review Letters* **100**, 57202 (2008).
- ⁹⁵ Z. Wang, J. Wu, W. Yang, A. K. Bera, D. Kamenskyi, A. T. M. N. Islam, S. Xu, J. M. Law, B. Lake, C. Wu, and A. Loidl, *Nature* **554**, 219 (2018).
- ⁹⁶ O. E. Alon, V. Averbukh, and N. Moiseyev, *Physical Review Letters* **80**, 3743 (1998).
- ⁹⁷ B. A. Ruzicka, L. K. Werake, G. Xu, J. B. Khurgin, E. Y. Sherman, J. Z. Wu, and H. Zhao, *Physical Review Letters* **108**, 77403 (2012).
- ⁹⁸ A. Moor, A. F. Volkov, and K. B. Efetov, *Physical Review Letters* **118**, 47001 (2017).
- ⁹⁹ S. Nakamura, Y. Iida, Y. Murotani, R. Matsunaga, H. Terai, and R. Shimano, *Physical Review Letters* **122**, 257001 (2019).
- ¹⁰⁰ B. K. Chakrabarti, A. Dutta, and P. Sen, *Quantum Ising Phases and Transitions in Traverse Ising Models* (Springer Nature, 1996).
- ¹⁰¹ J. R. Schrieffer, *Theory Of Superconductivity* (Westview Press, 1971).
- ¹⁰² M. Tinkham, *Introduction to Superconductivity: Second Edition* (Dover Publications, 2004).
- ¹⁰³ In the case of $|g_u| \leq 1$, in addition to $|\Psi_{\Pi}\rangle$ of Eq. (31), there exists an almost degenerate state in the subspace of states with odd fermion numbers: $|\Psi'_{\Pi}\rangle = \hat{d}_{\pi}^{\dagger} \prod_{0 < k < \pi} (u_k + v_k \hat{d}_k^{\dagger} \hat{d}_{-k}^{\dagger}) |0\rangle$ with $k = \pi m/L$ ($m = 1, 2, \dots, L-1$). These states $|\Psi_{\Pi}\rangle$ and $|\Psi'_{\Pi}\rangle$ are eigenstates of the global π rotation around the S^z axis \hat{U}_{π}^z , $\hat{U}_{\pi}^z \hat{S}_j^{\alpha} \hat{U}_{\pi}^{z\dagger} = -\hat{S}_j^{\alpha}$ ($\alpha = x, y$), with eigenvalue 1 and -1 , respectively. Meanwhile, the two Néel states $|\mathcal{N}_{+}\rangle = |\rightarrow\leftarrow\rightarrow\cdots\rangle$ and $|\mathcal{N}_{-}\rangle = |\leftarrow\rightarrow\leftarrow\cdots\rangle$ in the thermodynamic limit satisfy $\hat{U}_{\pi}^z |\mathcal{N}_{\pm}\rangle = |\mathcal{N}_{\mp}\rangle$. Thus $|\Psi_{\pm}\rangle \equiv (|\Psi_{\Pi}\rangle \pm |\Psi'_{\Pi}\rangle)/\sqrt{2}$ satisfying $\hat{U}_{\pi}^z |\Psi_{\pm}\rangle = |\Psi_{\mp}\rangle$ correspond to the Néel states. Nevertheless, for large system sizes, all these states lead to almost the same dynamics for \hat{M}_z because $\langle\Psi'_{\Pi}|\hat{M}_z(t)|\Psi_{\Pi}\rangle = 0$ and $\langle\Psi_{\Pi}|\hat{M}_z(t)|\Psi_{\Pi}\rangle \simeq \langle\Psi'_{\Pi}|\hat{M}_z(t)|\Psi'_{\Pi}\rangle$, where $\hat{M}_z(t)$ is the Heisenberg-picture operator.
- ¹⁰⁴ E. Saitoh, M. Ueda, H. Miyajima, and G. Tatara, *Applied Physics Letters* **88**, 182509 (2006).
- ¹⁰⁵ T. Kimura, Y. Otani, T. Sato, S. Takahashi, and S. Maekawa, *Phys. Rev. Lett.* **98**, 156601 (2007).
- ¹⁰⁶ S. O. Valenzuela and M. Tinkham, *Nature* **442**, 176 (2006).